Engineering Geology 325 (2023) 107278

Contents lists available at ScienceDirect

Engineering Geology

journal homepage: www.elsevier.com/locate/enggeo

# Plume effects on Martian surface: Revealing evolution characteristics of plume-surface interaction at Tianwen-1 landing site

Pengwei Luo [a,c,1], Xiaoping Zhang [a,c,*], Renrui Liu [a,c,1], Mingjie Zhang [a,c], Cunhui Li [b,h,*], Yi Xu [a,c], Roberto Bugiolacchi [a,c], Baocheng Hua [d,e], Haiyan Zhang [b,i], Liansheng Li [d,e], Jilin You [a,c], Yanyan Xu [a,c], Lei Lei [a,c], Xin Zou [f], Qingfei Fu [g], Yi Wang [b], Xiao Liang [d,e], Jianhong Zhuang [b], Li Wang [d,e,*], Yuming Wang [h], Weidong Wang [i], Linping Feng [j], Haiwen Liu [j], Tao Li [d,e]

[a] State Key Laboratory of Lunar and Planetary Sciences, Macau University of Science and Technology, Macau 999078, China
[b] Science and Technology on Vacuum Technology and Physics Laboratory, Lanzhou Institute of Physics, Lanzhou 730000, China
[c] CNSA Macau Center for Space Exploration and Science, Macau 999078, China
[d] Space Optoelectronic Measurement and Perception Lab, Beijing Institute of Control Engineering, Beijing 100190, China
[e] Science and Technology on Space Intelligent Control Laboratory, Beijing Institute of Control Engineering, Beijing 100190, China
[f] Beijing Institute of Spacecraft System Engineering, China Academy of Space Technology, Beijing 100094, China
[g] School of Astronautics, Beihang University, Beijing 100191, China
[h] School of Earth and Space Sciences, University of Science and Technology of China, Hefei 230026, China
[i] School of Mechano-Electronic Engineering, Xidian University, Xi'an 710071, China
[j] School of Electronic and Information Engineering, Xi'an Jiaotong University, Xi'an 710049, China

## ARTICLE INFO

*Keywords:*
Tianwen-1 mission
Zhurong rover
Shallow stratigraphic architecture
Plume-surface interaction

## ABSTRACT

Engine plumes can seriously erode the Martian surface during the landing phase, causing a substantial alteration of the terrain of the immediate touchdown area and beyond. Furthermore, large amounts of lifted dust can block the view of boulders or craters, posing a serious threat to the lander's safety. Improving our understanding of the plume-surface interaction can reduce the risk of failure on a Mars landing mission. In situ studies on this subject are limited, particularly those relating to high-thrust single-nozzle engines. The Tianwen-1 represents the only Mars landing mission that employed such an engine with a thrust of ~3000 N during the landing phase: Its success represents a unique opportunity in addressing this issue, providing an important reference for future Mars return missions. Here, we report the evolution characteristics of the plume-induced regolith erosion and the plume impingement effect measurements at the Tianwen-1 landing site. The results show that depressions and infilling are a complex process accompanying the changing of patterns as the lander descends. Specifically, the plume will seriously erode the area beneath the nozzle, causing the formation of a deep crater. Meanwhile, the expanding radial flow tends to flatten the peripheral area of the lander, which depends on the homogeneity of the regolith. To better quantify the impingement effects, some crucial parameters were extracted. The measured volume, diameter, and depth of the crater are 0.115 ± 0.019 $m^3$, 1.50 m, and ~0.35 m, respectively. We also calculated the total erosion area and volume as 4879.4 ± 297.7 $m^2$ and 376.9 ± 102.2 $m^3$. In addition, plume-induced infilling/erosion depths and rates during the landing phase were measured. Further, we investigated the shallow stratigraphic architecture exposed by the plume-induced crater beneath the lander, showing that it represents probably dust/sand-coated black rocks above at least ~35 cm thick, bright reddish materials. These results provide valuable insights into the plume impingement effects on the Martian surface and the shallow subsurface layer at the Tianwen-1 landing site, which will benefit future Mars explorations.

* Corresponding authors.
*E-mail addresses:* xpzhangnju@gmail.com (X. Zhang), licunhui@spacechina.com (C. Li), wupeng3992@163.com (L. Wang).
[1] These authors contributed equally to this work.

https://doi.org/10.1016/j.enggeo.2023.107278
Received 28 July 2022; Received in revised form 6 February 2023; Accepted 30 August 2023
Available online 1 September 2023

## 1. Introduction

The Moon and Mars are currently the two leading targets of interest in deep space exploration, given that they are deemed crucial stepstones toward expanding the potential human habitats. Unprotected by a meaningful atmosphere, the lunar surface has been directly exposed to space weathering for billions of years, impacted by micro- to macro-sized space debris (Horányi et al., 2014) and cosmic rays (Luo et al., 2022); surface rocks also experience extreme thermal expansion and contraction conditions within a day. The fragmented rocks and minerals eventually produce a thick layer of welded particles, called regolith (Spray, 2016), which increases in density with depth. The component particles are rough and angular rendering them highly frictional (Metzger et al., 2009a). Mars's distance from the Earth is between ~55 million to ~400 million kilometers. The planet is dry and desolate within the Solar System's habitable zone. It has near-surface water ice in places (Bandfield, 2007) and a thin atmosphere consisting of $CO_2$ (~ 95%), $N_2$ (~3%), and Ar (~2%) (Franz et al., 2017), with an average atmospheric pressure of about 1% of that on the Earth (Harri et al., 2014). Its atmosphere and the relatively benign thermal environment prevent the surface from enduring the same degree of space weathering and extreme thermal excursions as the Moon. The regolith particles on Mars are also geologically better sorted, resulting in a weaker and more porous upper regolith (Metzger et al., 2009a).

In situ Mars missions have been remarkable (Li et al., 2021a) and yielded great scientific returns, but rather more challenging to accomplish compared to the Moon. Indeed, since the 1960s, out of 48 Mars exploration missions, only 21 have been successful, including 10 landers, i.e., a success rate of 43.8% (https://mars.nasa.gov/mars-exploration/missions/historical-log/). Several technical and environmental reasons concur with this modest outcome, with two as the leading factors: the very long-distance hindering contemporaneous communication, and the presence of an atmosphere, which increases the landing complexity (Huang et al., 2021; Li et al., 2021b). This generally consists of three phases: entry, descent, and landing (EDL) (Huang et al., 2021): these are all quite complex and generally need to function autonomously without direct monitoring due to communication delays. To manage the potential risk factors and further improve the success rate of Mars landing missions, each phase should be understood thoroughly, particularly when missions with much larger landing weights will be developed, such as sample-return and human-class missions. The plume-surface interaction during the landing phase is one of these key research targets.

In general, the effects of the interaction between the plume and the landing area vary greatly with different conditions, such as the gravity of the planet, the mass and thrust of the lander, the porosity and mechanical strength of the soil, the density of the atmosphere, and the configuration of the engine (Watkins et al., 2021). As mentioned earlier, the physical characteristics of the Martian surface contrast substantially with the Moon, affecting the plume-surface interaction differently during the landing phase: this potentially hinders the results derived from the plume-lunar surface interaction from being directly applied to Mars. So far, several primary mechanisms by which gas interacts with surface materials have been identified: viscous erosion (VE) (Bagnold, 1941), bearing capacity failure (BCF) (Alexander et al., 1966), diffusion-driven flow (DDF) (Metzger et al., 2009b), diffused gas eruption (DGE) (Scott and Ko, 1968), and diffused gas explosive erosion (DGEE) (Mehta et al., 2011). As to the VE, the stand-off shockwave caused by the rocket exhaust striking the soil creates a stagnation zone (stationary gas) directly below the nozzle. As the hot gas moves away from the stagnation region, it expands and accelerates radially. VE is dominant on the lunar surface where loose materials can be easily scoured away by the plume expanding into the vacuum. In the case of the BCF, the jet exhaust from rockets has a high stagnation pressure that exceeds the bearing capacity of the soil, producing ground depressions. This occurs when jet exhaust pushes the soil down more rapidly than it can equilibrate. In contrast to the BCF, the DDF occurs when the soil is pushed down slower than the subsurface pressure develops (Metzger et al., 2009b). Regarding the DGE, exhaust gases diffuse into the soil between the grains of sand and dust. This builds up pressure to match the rocket exhaust on top of the soil. Therefore, the eruption can occur in two ways: (1) As it diffuses laterally under the surface, it builds up pressure away from the rocket centerline, causing a force imbalance that results in the eruption of the soil; (2) After shutting off the rocket engine, soil erupts along the engine's centerline toward the bottom of the rocket as a consequence of the sudden loss of pressure above the surface. DGE is generally important on small bodies such as asteroids. Considering the relatively low gas permeability and the large internal friction of the lunar regolith, the BCF, DDF, and DGE have a minimal impact on the lunar surface. On the contrary, the Martian ambient atmosphere confines the expanding plume to form a jet, which impinges on the loose Martian regolith to excavate a crater by the BCF, DDF, or a combination of the BCF and DDF mechanisms, causing a deep and large crater to form (Metzger et al., 2009a; Morris et al., 2012), in particular in the case of a human-class lander size. The atmosphere also inhibits the motion of dust as particles travel into the far field, which occurrence is not mirrored on the Moon (Mehta et al., 2011; Metzger et al., 2009a; Morris et al., 2012) due to its environment. DGEE is a mechanism discovered by Mehta et al. (2011) while studying the plume effects caused by the pulsed thrusters of the Mars Phoenix lander and only works with pulsed thrusters. In their scaled experiments, repeated shock waves were propagated through the subsurface of the regolith by the pulsed engines used by the Phoenix propulsion system. The kinetic energy as well as pressure gradients generated in the subsurface resulted in regolith losing shear strength, resulting in craters forming in the subsurface. They found that supersonic pulsed jet impingement may lead to erosion rates up to an order of magnitude higher than other processes induced by jets. In short, erosion is caused by the interaction between the plume and the soil. Essentially, erosion occurs when the static pressure of the plume exceeds the shear strength of the soil. When the lander's height is relatively large, the static pressure of the plume on the surface is relatively low, and erosion is dominated by the VE. With the gradual decrease in the lander's height, the static pressure increases. The dominant mechanism gradually shifts to the BCF, DDF, etc., depending on the conditions mentioned earlier.

However, several detrimental conditions may be triggered by the plume-surface interaction, including the alteration of the local terrain and the lander itself (Fontes and Metzger, 2022; Golombek et al., 2020; Hoey et al., 2020; Immer et al., 2011; Lane and Metzger, 2015a; Metzger et al., 2011; Plemmons et al., 2008; You et al., 2021). Soil and dust can also be blown by the engine exhaust in horizontal sheets along the surface away from the lander and the resultant opaque sheet can block the view of boulders or craters (Lane and Metzger, 2015b; Metzger et al., 2011; You et al., 2021), posing a serious threat to the lander's safety. In addition, the crater excavated by the erosion process could subsequently collapse into a larger residual crater when the engine shuts off, and the enlarged crater may sap soil beneath the lander's footpads and tilt the lander (Metzger, 2016). Further, sensitive instrument surfaces can be contaminated by exhausted gas and liquid propellant by-products, potentially impacting the science outcome (Hoey et al., 2020). More plume-induced detrimental conditions can be found in the literature and the references therein. (e.g., Vizcaino and Mehta, 2015). Consequently, estimating the plume impingement effects at the landing site is of paramount importance, which includes determining the total area and volume eroded by the plume. In addition, measurements are made of the volume, diameter, and depth of the residual crater beneath the lander excavated by the plume. To minimize the risks associated with these adverse factors, it is also essential to conduct a plume-induced regolith erosion evolution process study to determine the optimal engine shut-off height under a specific configuration.

Li et al. (2022) produced a detailed subsurface image profile using data from the low-frequency radar onboard the Zhurong rover. It shows an approximately 70-m-thick, multilayered structure beneath a < 10-m-thick regolith layer. There is, however, a high level of contamination in the top part of the low-frequency radar profile, likely caused by multiple reflections between the rover and the ground surface, which makes it difficult to determine the base of this top layer and how it separates from the underlying materials. In this case, it is apparent that no stratigraphic information is provided for the shallow subsurface layer. As a complement to the radar data, the shallow stratigraphic architecture of the landing site exposed by plume-induced erosion could provide potential material information of the Martian subsurface.

On May 15, 2021, the Tianwen-1 lander successfully landed on the surface of Mars. The Tianwen-1 landing site (25.066°N, 109.925°E) (Wan et al., 2021) is located in the southern Utopia Planitia on Mars at an elevation of −4099.8 m, as shown in Fig. 1. The landing site is flat with a low slope of 0 to 0.55° within a radial distance of 5 km from the lander. The landing region lies in the Late Hesperian lowland unit (lHl) (Tanaka et al., 2014). This unit mainly consists of the Vastitas Borealis Formation (VBF) materials, which were proposed as fluvial or marine sedimentary deposits (Kreslavsky and Head, 2002; Tanaka, 2005). Various geomorphologic features are found in this region, including aeolian bedforms, pitted cones, mesas, polygon troughs, ridges, ghost craters, rocky ejecta craters (RECs) and pitted-wall craters (Wu et al., 2021; Ye et al., 2021; Zhao et al., 2021). The pitted cones, polygon troughs and pitted-wall craters potentially provide insights into the presence of volatiles. The findings of hydrated minerals in some platy rocks by Zhurong (Liu et al., 2022) further attest to the existence of ancient aqueous activity. Platy-like duricrusts thought to be developed locally are also observed along the Zhurong rover's traverse path.

Due to the scarcity of in-situ data, laboratory and numerical simulations have been extensively used to understand the plume-surface interaction on Mars (e.g., Mehta et al., 2013; Metzger et al., 2009a). Currently, the data on the plume-surface interaction on Mars mainly derives from ground experiments and observations from multiple Mars landers/rovers, such as Vikings (e.g., Shorthill et al., 1976a; Shorthill et al., 1976b; Hutton et al., 1980), Phoenix (e.g., Mehta et al., 2011; Sizemore et al., 2010; Smith et al., 2009), InSight (e.g., Golombek et al., 2020; Warner et al., 2022), and Curiosity (Mars Science Laboratory, MSL) (e.g., Vizcaino and Mehta, 2015). However, the simulations and ground experiments can only approach the complexity of a real case scenario. During their landing phase, the Viking-1 and Viking-2 landers, as well as the Curiosity rover, used non-pulsed thrusters, while the Phoenix and InSight landers employed pulsed thrusters instead. All the landers/rovers listed above used relatively low-thrust multiple-nozzle engines (dozens to several hundred newtons per nozzle). Considering that loads of future sample-return missions, human-class missions particularly, will be much larger, a thorough in situ study on the plume-surface interaction based on the observations from a mission using a high-thrust single-nozzle engine becomes important. Using a non-pulsed single-nozzle engine with high thrust (approximately 3000 N during the landing phase) (Han et al., 2022) and a hovering and obstacle avoidance landing strategy, Tianwen-1 offers a unique opportunity to study the topics mentioned above.

The Tianwen-1 is powered by a throttleable descent engine with a maximum thrust of approximately 7500 N and the nozzle is located at the center of the lander's bottom with a 0.233 m outlet diameter. More information about the Tianwen-1 Mars lander propulsion system can be found in the literature (Han et al., 2022). The lower edge of the circular chassis of the Tianwen-1 lander is equipped with two identical optical obstacle avoidance cameras (hereinafter referred to as landing cameras) (Hua et al., 2022), which are installed symmetrically relative to the engine nozzle center of the lander. During the slow landing phase, this pair of landing cameras can take pictures of the approaching terrain simultaneously. In addition, the Zhurong rover carries six scientific payloads, including the Navigation and Terrain Cameras (NaTeCams) (Liang et al., 2021) and the Mars Rover Penetrating Radar (RoPeR) (Zhou et al., 2020). From these datasets, our aim is to: (i) study the evolution process of plume-surface interaction based on the landing images, including the determination of the optimal engine shut-off height from the perspective of plume-surface interaction and the estimation of infilling/erosion depth and rate by using images taken at adjacent points in time; (ii) measure the plume impingement effects, including the estimation of the total plume-induced erosion area and

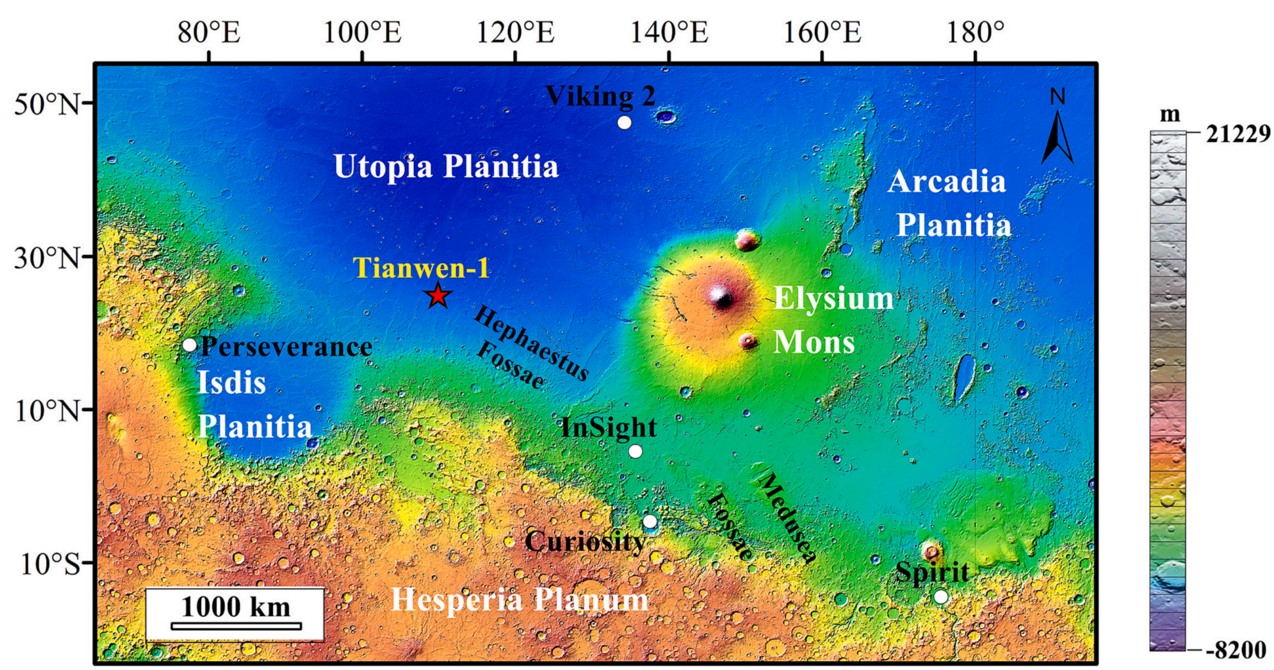


**Fig. 1.** Topographic map of the area around the Tianwen-1 lander, displaying the physiographic features and landing sites of the Tianwen-1 lander (red pentagram), Perseverance rover, Viking-2 lander, Insight lander, Curiosity rover, and Spirit rover (white points). The base map is a MOLA (Mars Orbiter Laser Altimeter) shaded-relief topographic map of Mars (https://astrogeology.usgs.gov/search/map/Mars/GlobalSurveyor/MOLA/Mars_MGS_MOLA_ClrShade_merge_global_463m). (For interpretation of the references to color in this figure legend, the reader is referred to the web version of this article.)

volume at the landing site by analyzing the image data from the NaTeCams, the High Resolution Imaging Science Experiment (HiRISE) (McEwen et al., 2007) onboard the Mars Reconnaissance Orbiter (MRO) (Zurek and Smrekar, 2007), and the High Resolution Imaging Camera (HiRIC) (Meng et al., 2021) onboard the Tianwen-1 orbiter, the determination of the volume, diameter, and depth of the residual crater excavated by the plume with the images from NaTeCams, and the investigation into the shallow stratigraphic architecture of the Tianwen-1 landing site based on the landing images and the images taken by the NaTeCams.

## 2. Results

### 2.1. Evolution characteristics of plume-surface interaction during the landing phase

Digital Elevation Models (DEMs) of the touchdown area were derived from images taken by the landing cameras. The differences of the reconstructed DEMs at two adjacent lander heights are also presented to investigate the evolution characteristics of the plume-Martian surface interaction (Figs. 3 and 4). The reconstructed DEMs of the landing area at heights of $H_3 = 9.161 \pm 0.024$, $H_2 = 15.791 \pm 0.022$, and $H_1 = 31.450 \pm 0.038$ m are shown as the top panels in Figs. 3 and 4, respectively, while the differences of the DEMs at two adjacent lander heights are shown below. Note that the local surface of the landing area is relatively uneven at $H_1 = 31.450 \pm 0.038$ m with respective depth ranges of (−0.015 to 0.072) and (−0.093 to 0.090) m in the field of view

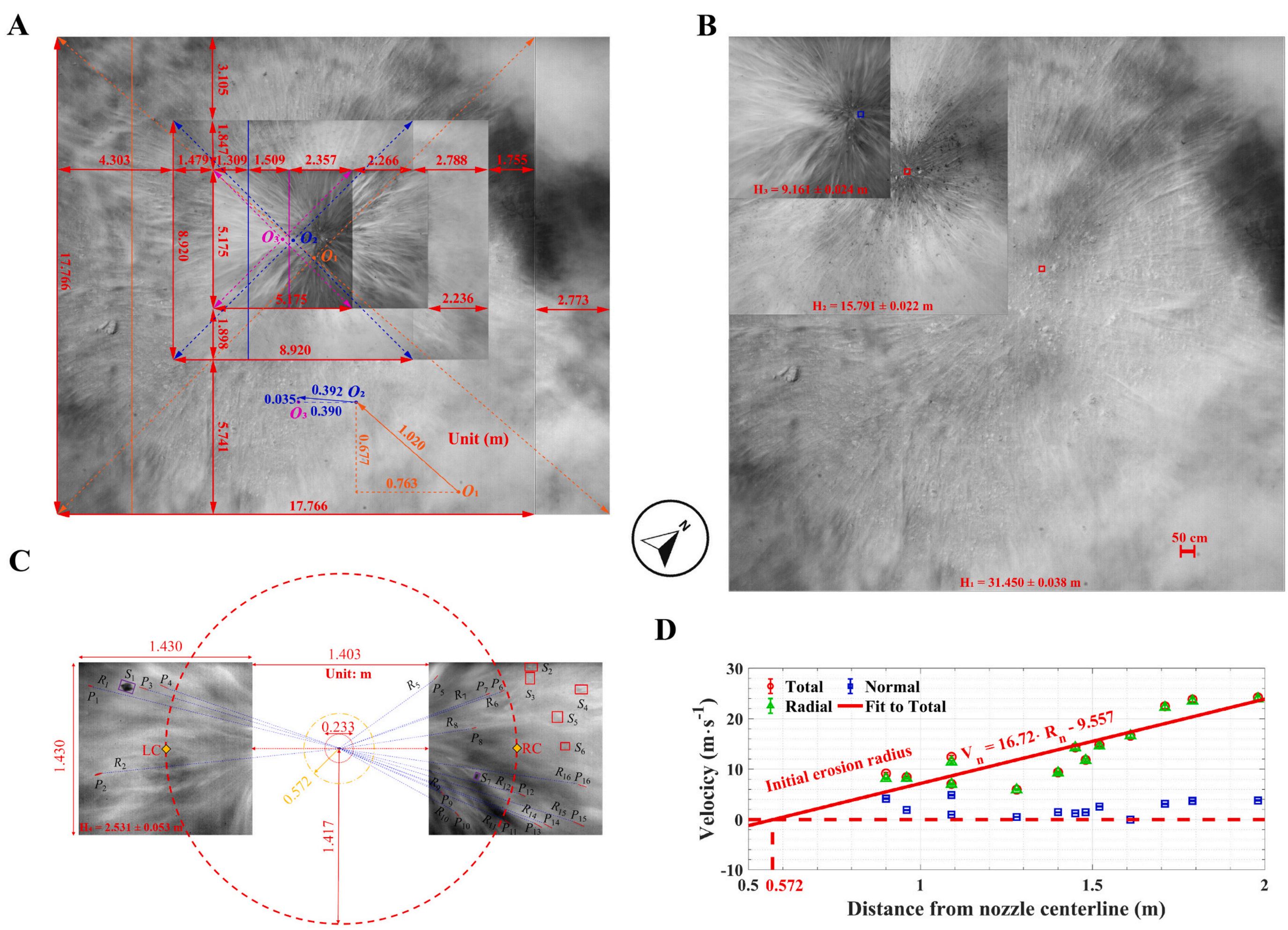


**Fig. 2.** Alignment of the landing images and the relationship between the particle velocity and the distance of the particle from the nozzle centerline. (A) The relative positions of the engine nozzle centerlines at different heights between $H_1 = 31.450 \pm 0.038$ and $H_3 = 9.161 \pm 0.024$ m, where $O_1$ (orange color), $O_2$ (blue color), and $O_3$ (purple color) are the projections of the nozzle center points at heights $H_1 = 31.450 \pm 0.038$, $H_2 = 15.791 \pm 0.022$, and $H_3 = 9.161 \pm 0.024$ m, respectively. (B) The landing images taken by the left camera at different shooting heights along with the fixed reference point at different heights enclosed by solid boxes. (C) The relative position of the lander and the landing images at a height of $H_4 = 2.531 \pm 0.053$ m. The larger red dashed circle represents the outline of the lander, whereas the outline of the nozzle and the initial erosion radius are indicated by the small red dotted and the yellow dash-dotted circles, respectively. The diamonds filled in orange color indicated by LC and RC represent the left and the right landing cameras, respectively. $P_n$ and $R_n$ represent the $n$th particle and its corresponding distance from the nozzle centerline, respectively, where $n = 1, 2, 3, \ldots, 16$. $S_n$ enclosed by a violet dashed box is a flying particle almost at a standstill, while that enclosed by a red dashed box is a motionless big rock/granule with the radius of an equivalent circle in the range of ~2 to ~4 cm on the Martian surface, where $n = 2, 3, \ldots, 6$. (D) The particle velocity ($V_n$) and the distance between the particle (the diameters of these particles are in the range of ~7 to ~9 mm) and the nozzle centerline ($R_n$) are in linear relationship fitted by $V_n = 16.72 \cdot R_n$ - 9.557 ($n > 2$), where $V_n$ and $R_n$ are in units of m/s and m, respectively. Note that the landing images in (A), (B) and (C) have been scaled with the corresponding lander heights when shooting. (For interpretation of the references to color in this figure legend, the reader is referred to the web version of this article.)

at heights $H_3 = 9.161 \pm 0.024$ (Fig. 3C) and $H_2 = 15.791 \pm 0.022$ m (Fig. 4B), showing that, as a general trend, the terrain is higher in the area beneath the lander and lower around it. As the lander descends, the surface tends to be flattened by the plume-surface interaction, and accordingly, the depth range at the height of $H_2 = 15.791 \pm 0.022$ m is changed from (−0.093 to 0.090) to (−0.059 to 0.076) m in the field of view at height $H_2 = 15.791 \pm 0.022$ m (Fig. 4A). The terrain has become much flatter than it was at the previous height $H_1 = 31.450 \pm 0.038$ m, particularly beneath the lander (Fig. 4A). It is evident that high-lying areas are eroded while low-lying ones are infilled, which can be attested by looking at the difference between the reconstructed DEMs at two adjacent lander heights (Figs. 3E and 4C). Of note, the areas with negative depth differences are eroded while those with positive ones are infilled. At the height of $H_1 = 31.450 \pm 0.038$ m, only parts of the areas

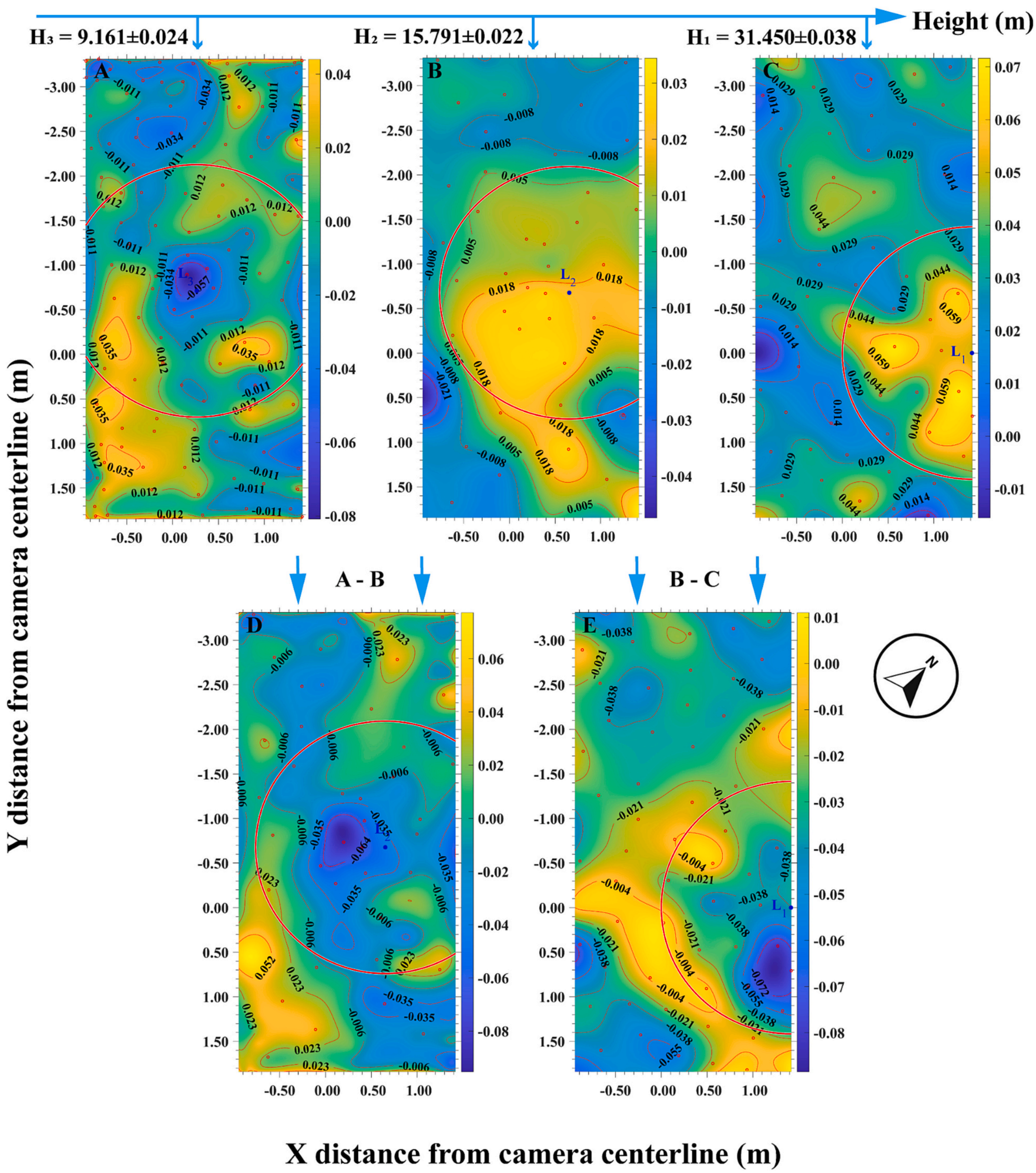


**Fig. 3.** DEM reconstruction of the local landing area based on the landing images at different heights in the field of view at height $H_3 = 9.161 \pm 0.024$ m. The large red circle in each plot denotes the outline of the lander. The feature points used to determine the height of the lander are indicated by small red circles. Plots upwards (A to C) show the DEMs of the landing area at different lander heights in the common field of view of the landing cameras at a height of $H_3 = 9.161 \pm 0.024$ m, and the differences of the DEMs at two adjacent lander heights are shown in the plots downwards (D and E), where the difference values in positive correspond to the region being filled with the decrease of the lander height while for those in negative the opposite is true. (For interpretation of the references to color in this figure legend, the reader is referred to the web version of this article.)

near the edges of the landing cameras' field of view are affected by plume-induced fine-grained particles. As the lander's height decreases to $H_2 = 15.791 \pm 0.022$ m, fine-grained particles have a marginal impact on the visibility, which is attributed to the shrinking of the cameras' field of view. The VE mechanism prevails between these two heights as evidenced by the radial streaks, and contributes slightly to the formation of a crater. Similarly, radial streaks can also be seen at $H_3 = 9.161 \pm 0.024$ m and the cameras' field of view further shrinks. However, the plume intensely erodes the area under the nozzle, resulting in the formation of an 8.1-cm-deep crater beneath the lander (see the area in dark blue color near the projection point of the nozzle center $L_3$ in Fig. 3A), which is demonstrated further in Fig. 3D. Fine-grained particles, accompanied by debris and ejecta material, significantly obscure the view of the landing cameras. At $H_3 = 9.161 \pm 0.024$ m, both BCF/DDF and VE mechanisms dominate. The flatness of the terrain as in Fig. 3A decreases compared to that in Fig. 3B, possibly resulting from the inhomogeneity of regolith. Fig. 2B illustrates that the surface is embedded with clasts ranging in size from pebbles to cobbles, and that the clasts are unevenly distributed throughout the regolith. Material could also accumulate around some exposed motionless clasts, resulting

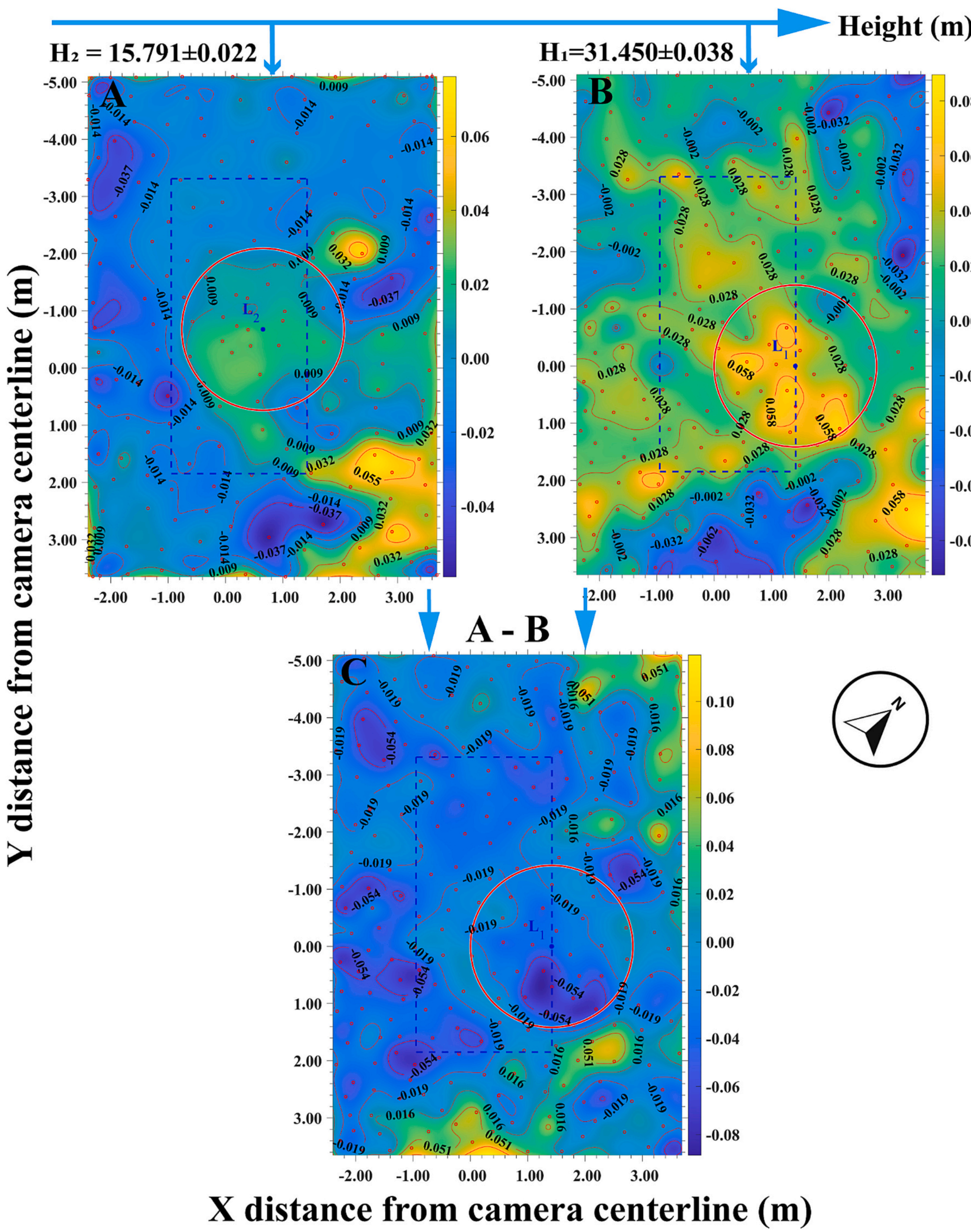


**Fig. 4.** Similar to Fig. 3, but are in the common field of view of the landing cameras at a height of $15.791 \pm 0.022$ m. The dashed rectangle in blue corresponds to the field of view in Fig. 3. (For interpretation of the references to color in this figure legend, the reader is referred to the web version of this article.)

in local elevations. Additionally, plate-like duricrusts were found along the Zhurong rover's traverse path (Liu et al., 2022). Such a structure may be common at the landing site, whose distribution may also affect the terrain's flatness. Accordingly, the depth range at the height of $H_3 = 9.161 \pm 0.024$ m is changed from (−0.047 to 0.034) to (−0.081 to 0.044) m in the field of view at height $H_3 = 9.161 \pm 0.024$ m (Fig. 3A). At the height of $H_4 = 2.531 \pm 0.053$ m, the surface is completely obscured by debris and ejecta material beneath the lander, and the BCF/DDF dominates at this height. Thus, from the perspective of plume-surface interaction, the optimal engine shut-off height for Tianwen-1 is ~15 m and the lander height during hovering and obstacle avoidance should be larger than ~31 m. Further conclusions are made regarding the plume-surface interaction of the local terrain beneath the lander: The plume ejected from the nozzle will erode the area below it considerably, causing this area to sink ever lower until a deep crater develops. Additionally, the radial flow tends to flatten the peripheral area of the lander, although, the flatness depends on the homogeneity of the regolith.

In addition, differencing DEMs can be challenging because a slight difference in their reference planes may result in a large difference in volume calculation. Note that the reference plane here refers to the plane used to determine the base elevations to obtain the DEMs in Figs. 3 (A to C) and 4 (A to B) (see the red dashed line in Fig. S1B and the main text in supplementary materials for details). Finding a fixed reference point in the landing images taken at adjacent heights is a reliable way to determine their respective base elevations. Consequently, we attempt to determine the base elevations at these three shooting heights. In Fig. 2B, the landing images taken by the left landing camera at these three shooting heights are shown along with their fixed reference point (solid boxes). Of note here is that all these images are scaled according to their corresponding shooting heights, which are calculated by averaging the elevation values of their respective selected feature points (small red circles in Figs. 3 and 4). A fixed reference point (enclosed by red solid boxes in Fig. 2B) is chosen based on the overlap between landing images taken at heights of $H_1 = 31.450 \pm 0.038$ and $H_2 = 15.791 \pm 0.022$ m. As for the heights at $H_2 = 15.791 \pm 0.022$ and $H_3 = 9.161 \pm 0.024$ m, the fixed reference point is difficult to find in their respective landing images due to the intense plume-surface interaction during the landing phase. The positions enclosed by the blue and red solid boxes are corresponding (Fig. 2B). Obviously, the area enclosed by the blue solid box is eroded. To determine the base elevation in this case, the average elevation of selected feature points is used instead. To verify the reliability of the substitution, we calculate the elevation difference between the heights at $H_1 = 31.450 \pm 0.038$ and $H_2 = 15.791 \pm 0.022$ m based on their fixed reference point shown in Fig. 2B in comparison with that obtained from their average elevation values of selected feature points. The former is calculated to be 15.658 m, and the latter is 15.659 m with a slight difference of 1.0 mm. It can therefore be concluded that the substitution is relatively reliable. It should be pointed out that the DEMs in Figs. 3 and 4 are derived from the base elevations obtained by averaging elevation values of their respective selected feature points. Moreover, the relative position of the landing images taken at $H_2 = 15.791 \pm 0.022$ and $H_3 = 9.161 \pm 0.024$ m is determined from the flow-induced radial ridges and troughs away from the lander (Fig. 2). It is also important to mention that there are horizontal displacements during the lander descent, where the relative positions of the engine nozzle centerlines at different heights between $H_1 = 31.450 \pm 0.038$ and $H_3 = 9.161 \pm 0.024$ m are shown in Fig. 2A (the projections of the nozzle center points at heights $H_1 = 31.450 \pm 0.038$, $H_2 = 15.791 \pm 0.022$, and $H_3 = 9.161 \pm 0.024$ m are indicated by $O_1$ (orange color), $O_2$ (blue color), and $O_3$ (purple color), respectively). Note that these horizontal displacements are considered when extracting the differences of the adjacent DEMs at different lander heights.

We also extract the weighted average infilling/erosion depth and rate between two adjacent shooting heights, as shown in Tables 1 and 2. The weighted average infilling and erosion depths [rates] from $H_1 = 31.450 \pm 0.038$ to $H_2 = 15.791 \pm 0.022$ m in the common field of view at $H_2 = 15.791 \pm 0.022$ m (Fig. 4C) are calculated as 0.860 ± 0.037 [3.01 ± 0.13] and 3.01 ± 0.11 cm [10.55 ± 0.37 kg · (s · m$^2$)$^{-1}$], respectively, while those in the common field of view at $H_3 = 9.161 \pm 0.024$ m (Fig. 3E) are 0.0310 ± 0.0098 [0.108 ± 0.034] and 6.17 ± 0.21 cm [21.61 ± 0.73 kg · (s · m$^2$)$^{-1}$]. As for those from $H_2 = 15.791 \pm 0.022$ to $H_3 = 9.161 \pm 0.024$ m in the common field of view at the height of $H_3 = 9.161 \pm 0.024$ m (Fig. 3D), they are separately determined to be 1.84 ± 0.46 [6.46 ± 1.63] and 2.80 ± 0.61 cm [9.80 ± 2.15 kg · (s · m$^2$)$^{-1}$]. As mentioned earlier, the determination of base elevations matters. The base elevations of heights at $H_1 = 31.450 \pm 0.038$ and $H_2 = 15.791 \pm 0.022$ m can be accurately determined based on the fixed reference point in their corresponding landing images. However, determining the base elevations of the next adjacent heights at $H_2 = 15.791 \pm 0.022$ and $H_3 = 9.161 \pm 0.024$ m based on the same method is infeasible due to the intense plume erosion. In such a case, we float the base elevation of the height at $H_3 = 9.161 \pm 0.024$ m within a reasonable range and then take the weighted average of the results obtained within that range. Specifically, the weight is obtained based on the Gaussian distribution with parameters ($\mu = 9.161$ m, $\sigma = 0.005$ m). Considering that only a slight difference of 1.0 mm exists between the

**Table 2**
Similar to Table 1, but are between the adjacent shooting heights at $H_2 = 15.791 \pm 0.022$ and $H_3 = 9.161 \pm 0.024$ m in a specific FOV.

| Shooting height [m] | Infilling | | Erosion | |
|---|---|---|---|---|
| | Weighted average depth [cm] | Weighted average rate [kg· (s · m$^2$)$^{-1}$] | Weighted average depth [cm] | Weighted average rate [kg· (s · m$^2$)$^{-1}$] |
| | FOV-$H_3$ | FOV-$H_3$ | FOV-$H_3$ | FOV-$H_3$ |
| $H_2 = 15.791 \pm 0.022$ $H_3 = 9.161 \pm 0.024$ | 1.84 ± 0.46 | 6.46 ± 1.63 | 2.80 ± 0.61 | 9.80 ± 2.15 |

**Table 1**
The weighted average infilling/erosion depth and rate between the adjacent shooting heights at $H_1 = 31.450 \pm 0.038$ and $H_2 = 15.791 \pm 0.022$ m in a specific field of view (FOV). The infilling/erosion depth is defined as the quotient of the infilling/erosion volume and the area in the specific FOV. As for the infilling/erosion rate, it is defined as the product of the infilling/erosion depth and a constant equal to the quotient of the Martian regolith's bulk density and the shooting time interval. Further details about their definitions can be found in the supplementary materials. Note that FOV-$H_3$ and FOV–$H_2$ denote results derived from Figs. 3 and 4, respectively. The areas in the FOVs at heights $H_2 = 15.791 \pm 0.022$ and $H_3 = 9.161 \pm 0.024$ m are 36.98 and 5.61 m$^2$, respectively. The bulk density used to calculate the rate is ρ = 1.4 g/cm$^3$ (Krupenio, 1977; Shorthill et al., 1976c). The absolute values are taken for the weighted average erosion depth/rate.

| Shooting height [m] | Infilling | | | | Erosion | | | |
|---|---|---|---|---|---|---|---|---|
| | Weighted average depth [cm] | | Weighted average rate [kg· (s · m$^2$)$^{-1}$] | | Weighted average depth [cm] | | Weighted average rate [kg· (s · m$^2$)$^{-1}$] | |
| | FOV-$H_2$ | FOV-$H_3$ | FOV-$H_2$ | FOV-$H_3$ | FOV-$H_2$ | FOV-$H_3$ | FOV-$H_2$ | FOV-$H_3$ |
| $H_1 = 31.450 \pm 0.038$ $H_2 = 15.791 \pm 0.022$ | 0.860 ± 0.037 | 0.0310 ± 0.0098 | 3.01 ± 0.13 | 0.108 ± 0.034 | 3.01 ± 0.11 | 6.17 ± 0.21 | 10.55 ± 0.37 | 21.61 ± 0.73 |

elevation difference calculated based on their fixed reference point and the average elevations of their respective selected feature points at the last adjacent heights, $\sigma$ here is conservatively set to 5.0 mm. The base elevation of $H_3 = 9.161 \pm 0.024$ m varies in the range between 9.136 and 9.186 m with a step size of 0.005 mm. It is also necessary to point out that the same method is applied to the last adjacent heights at $H_1 = 31.450 \pm 0.038$ and $H_2 = 15.791 \pm 0.022$ m. Gaussian distribution with parameters ($\mu = 15.791$ m, $\sigma = 0.001$ m) and a step size of 0.001 mm are employed, and the base elevation ranges from 15.786 to 15.796 m. More details about the method are provided in the supplementary materials.

Besides, many particles are spurted out by the plume (Fig. 2C). To investigate the relationship between the particle velocity ($V_n$) and the distance between the particle and the nozzle centerline ($R_n$), we find some moving particles, which are denoted by $P_n$ ($n$=1, 2, 3, …, 16) in Fig. 2C. These particles with diameters ranging from ~7 to ~9 mm are indicated by $P_n$ with the subscripts of values $n > 2$, as shown in Fig. 2C. Scatter plots of $V_n$ vs. $R_n$ are displayed in Fig. 2D, which can be fitted with a linear function ($V_n = 16.72 \cdot R_n$ - 9.557 ($n > 2$), where $V_n$ and $R_n$ are in units of m/s and m, respectively). The tangential velocities of these particles are trivial and their radial velocities are dominant. The initial erosion radius at the shooting height of 2.531 $\pm$ 0.053 m is inferred to be 0.572 m indicated by the yellow dash-dotted circle and the red dashed line in Fig. 2 (C and D), respectively.

## 2.2. Plume impingement effect measurements

Figure 5A shows the patched 3D rendering of the Tianwen-1 landing area based on the terrain image data collected by the NaTeCams. The landing area images before and after the Tianwen-1 landing are displayed in Fig. 5 (B and C). The surface of the landing area is covered by relatively fine-grained particles (Fig. S14) with a relatively high albedo before the Tianwen-1 landing (Fig. 5B and Fig. 6B, Zone ④). During landing, the retrorocket expelled the surficial finer and brighter grains and exposed the underlying larger and darker grains, mainly composed of sand-sized particles in the range between 500 $\mu$m and 2 mm (Liu et al., 2022), producing a black blast zone of 60 to 150 m away around the lander (Zone ①) (Figs. 6B and S15). After landing, the Tianwen-1 lander vented the residual propellant using two engines with 250 N of thrust in the north and south directions, creating symmetrical jet-like albedo anomalies adjacent to the lander (Zones ② and ③). Around 0–7 [0–8] m

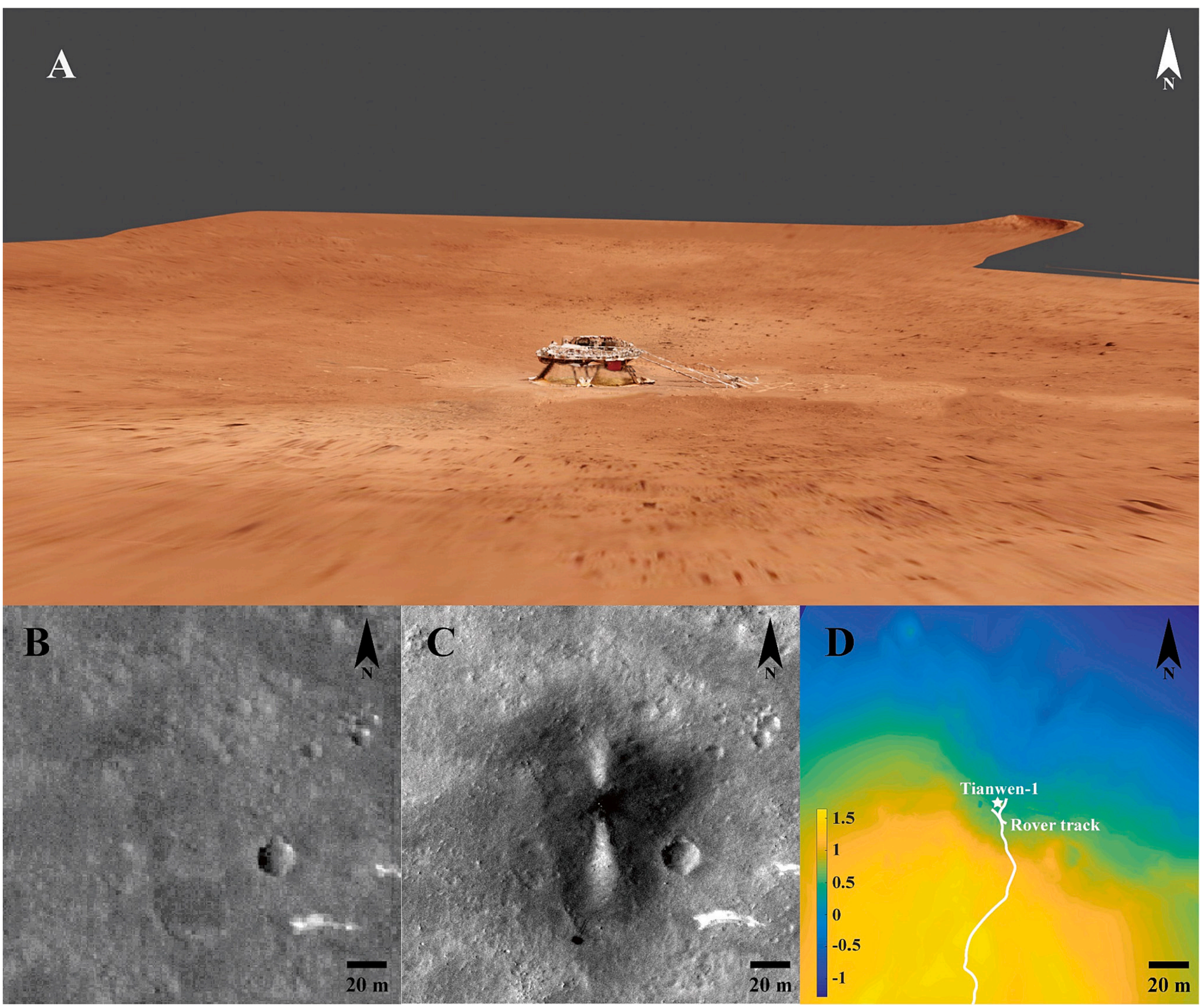


**Fig. 5.** DEMs reconstruction of the landing area based on the images taken by the NaTeCams and the high-altitude images from the HiRIC and the HiRISE onboard the Tianwen-1 orbiter and the MRO, respectively. (A) The patched 3D rendering of the Tianwen-1 landing area derived from the terrain image data collected by the NaTeCams. (B) The landing area image taken by the HiRIC before the landing of the Tianwen-1 lander. (C) Similar to (B), but was taken by the HiRISE after the Tianwen-1 landing. HiRISE images: ESP_069731_2055 (http://www.uahirise.org/ESP_069731_2055). (D) Orthographic DEM of the stereo model established based on the terrain image data from the NaTeCams with corrections.

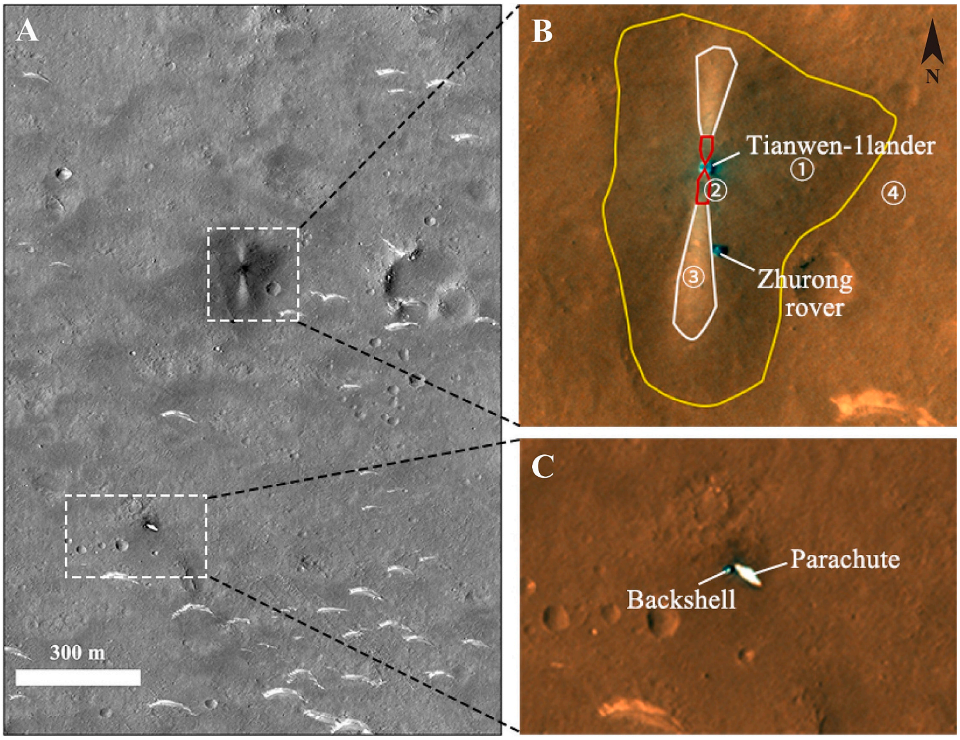


**Fig. 6.** Landing area images from the HiRISE. (A) A HiRISE image acquired on June 11, 2021, showing the location of (B) and (C). (B and C) The Tianwen-1 lander and Zhurong rover, and the parachute and backshell in color. HiRISE image: ESP_069731_2055 (http://www.uahirise.org/ESP_069731_2055). A schematic plot of the landing area divided into four types of zones indicated by the enclosed numbers is shown in (B). Note that Zones ② and ③ are enclosed by red and white solid lines, respectively. (For interpretation of the references to color in this figure legend, the reader is referred to the web version of this article.)

from the lander northwards [southwards], more darker grains, including many dark-toned rocks, were exposed by eroding resulting from the passivation process, further darkening Zone ②, as shown in Fig. S15, A to C (Zone ②, ~9 [~20] $m^2$ area). Note that the shape of Zones ② and ③ is very similar to that of the engine plume on the Martian surface (see Fig. 6B in this paper and Fig. 3 in the reference (Metzger et al., 2009a)). The sand-sized particles from Zone ② accumulated in Zone ③ (Fig. 6B and Fig. S15, B to D), brightening Zone ③ (~270 [~460] $m^2$ area), which extends from Zone ② out to ~7–37 [~8–51] m from the lander. This explanation is reasonable as demonstrated by the similarity of colors between Zone ③ and the dune (Fig. S15, B to D). By comparing the high-altitude images before and after landing, the total impacted area (Zones ① to ③) indicated by the image embedded in the upper right corner in Fig. 7A is estimated to be $4879.4 \pm 297.7$ $m^2$. Note that the impacted area is an average estimation based on four different selected areas (see the supplementary materials for details). The orthographic DEM of the stereo model derived from the terrain image data from the NaTeCams for the Tianwen-1 landing area is shown in Fig. 5D. To estimate the volume of the dust/grains blown off by the jet flow of the retrorocket, the DEM point cloud data of the Tianwen-1 landing area are processed as follows. First, we obtain the extended point cloud data of the impacted area before impingement by interpolation based on the point cloud data of the unimpacted area to extract the volume of the impacted area before impingement. Similarly, we can calculate the volume of the impacted area after impingement with the point cloud data obtained by interpolation. Then, by comparing the volumes of the impacted area before and after impingement, the total volume of the dust/grains blown off by the jet flow of the retrorocket can be calculated, as shown in Fig. 7 (D and E). The estimated volume of dust/grains blown off by the jet flow is $376.9 \pm 102.2$ $m^3$.

In addition, the stereo model of the residual crater created by the jet flow of the retrorocket under the lander is derived with the same methodology based on the selected images of the crater taken by the NaTeCams around the lander, as shown in Fig. 7B. The orthographic DEM of the crater stereo model is displayed in Fig. 7C. The volume of the crater is estimated at $0.115 \pm 0.019$ $m^3$, and the diameter and the depth of the residual crater are separately measured to be 1.50 m and about 0.35 m. It is important to point out that the diameter of the residual crater measured in this work is larger than that estimated (about 0.95 m diameter) in the literature (Ding et al., 2022). However, no specific estimation method is provided therein. In addition, Ye et al. (2022) studied the interaction between the plume and the Martian surface using a numerical simulation, showing that a residual crater with a 1.07 m diameter and a 0.33 m depth was created. The simulated diameter is smaller than our measurement, though the depth is close.

The morphology of the residual crater is displayed in the image embedded in the lower right corner of Fig. 7A. Overall, the residual crater is an inverted circular truncated cone in shape with the bottom edge more eroded in the southeast, forming a directional streak. There are two possible explanations for the formation of the streak: (1) The material in the area of the streak has a lower shearing strength, resulting in a stronger erosion. (2) Lateral movements occurred during the landing phase, causing erosion in the area corresponding to the streak. Here, we prefer the second explanation owing to the formation of the directional streak associated with erosion extending from the outside of the crater to its inside wall. Besides, there is no obvious difference between the streak and its surroundings in composition and in structure, as shown in Fig. 7 (A to C). We further compared the directions between the streak (Fig. 7C; southeast) and the lateral movements of the lander from $H_1 = 31.450 \pm 0.038$ to $H_3 = 9.161 \pm 0.024$ m (Fig. 2A; northeast), and found to be inconsistent. Therefore, we infer that the streak is formed by plume erosion under the height of $H_3 = 9.161 \pm 0.024$ m during landing. Furthermore, a clear groove is presented in Fig. 7A, as indicated by the black arrow in the lower right corner. The layer above the groove hollows out and is not broken, indicating that this layer has a certain shearing strength. Additionally, the exposed ~35 cm of the subsurface material appears to be abundant bright reddish, pebble to cobble-sized clasts (1–25 cm in diameter) within the fine-grained matrix or scattered within the crater. The pebbles and cobbles are equant to elongated in shape and in angular to subangular (Fig. S13). These observations suggest the shallow stratigraphic architecture at the Tianwen-1 is probably dust/sand-coated black rocks above at least ~35 cm-thick, bright reddish materials.

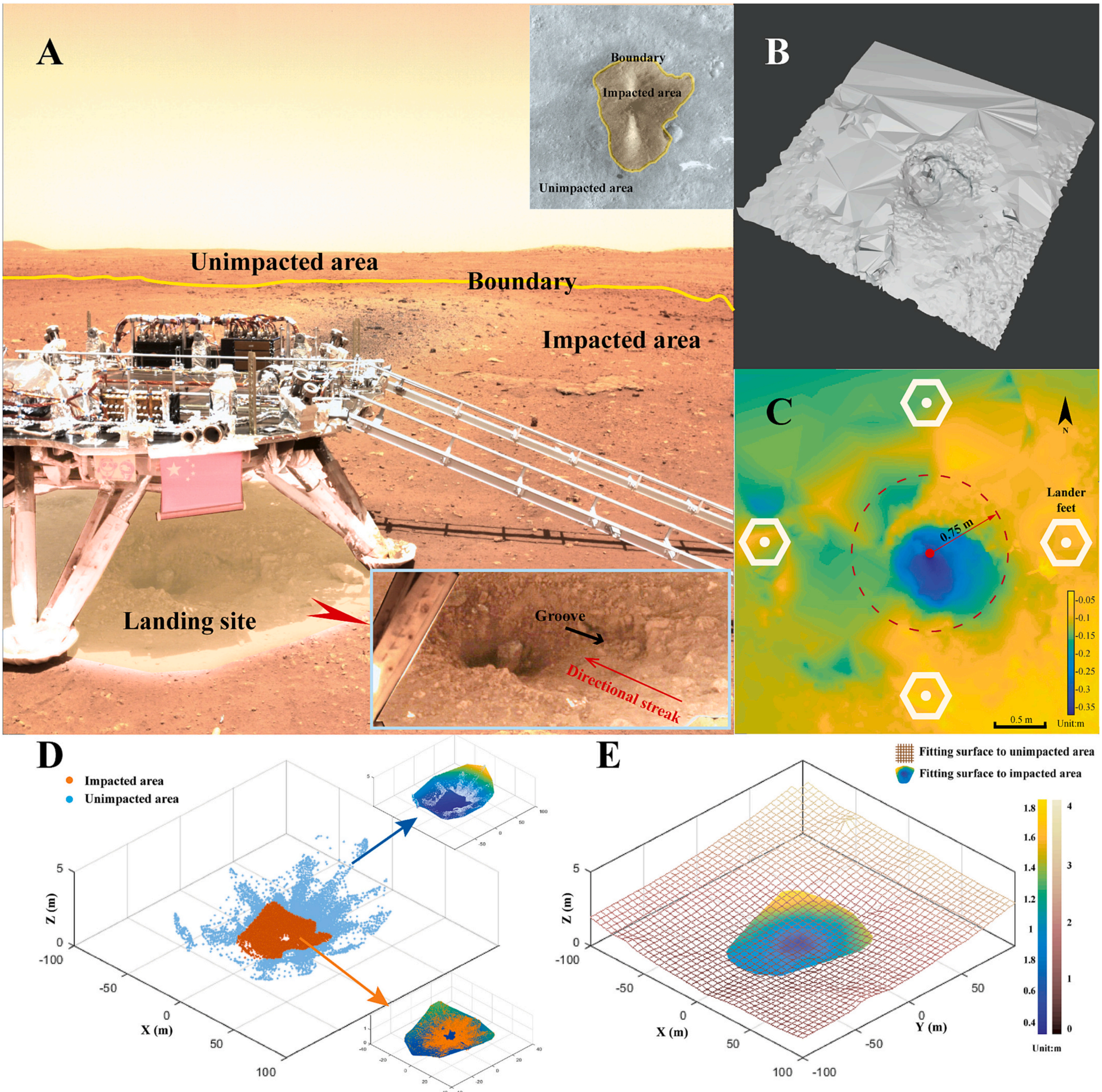


**Fig. 7.** DEM reconstruction of the residual crater under the lander with the images taken by the NaTeCams. (A) Photo of the landing site taken by the Zhurong rover, where the impacted area boundary and the crater excavated by the jet flow below the lander can be seen clearly. (B) Stereo model of the residual crater reconstructed based on the images from the NaTeCams. (C) Orthographic DEM of the residual crater under the lander, where the white hexagons denote the footpads of the lander, and the diameter of the red dashed circle indicates the size of the residual crater. (D) Point cloud data of the whole landing area, where the impacted and unimpacted areas are highlighted in orange and blue colors, respectively, and interpolation is applied separately to these two data sets indicated by the orange and the blue one-way arrows to obtain their corresponding extended surface. (E) Two extended surfaces are flattened to calculate the volume of the dust/grains blown off by the jet flow of the retrorocket. (For interpretation of the references to color in this figure legend, the reader is referred to the web version of this article.)

## 3. Discussion and conclusions

The plume-induced effects seriously threaten the safety of the lander. To eliminate these potential hazardous factors to the mission, one of the potential ways is to optimize the configuration of the engine. Mars missions have used two types of thrusters, pulse and non-pulse types. Thrusters can be further subdivided into single-nozzle and multiple-nozzle modes. Based on the available data, the plume erosion effects of a number Mars landing missions were compared.

To date, pulsed thrusters have been used only on the Phoenix (e.g., Mehta et al., 2011; Sizemore et al., 2010; Smith et al., 2009) and InSight (e.g., Golombek et al., 2020; Warner et al., 2022) missions. Their thrusters were all in multiple-nozzle mode. The Phoenix lander is equipped with 12 pulsed engines (~130 N per nozzle), causing a soil erosion depth from 5 to 18 cm and the exposure of the subsurface ice under the lander (with a radius between 75 and 85 cm from its centerline) (Mehta et al., 2011; Sizemore et al., 2010; Smith et al., 2009). Note that the hard ice layer prevented the plume from eroding further, which would have caused even more erosions. The InSight lander, with the same thruster as that equipped in the Phoenix lander, excavated three ~50 cm diameter and ~10 cm deep craters (Golombek et al., 2020). As for Viking landers, three non-pulsed 18-nozzle mono-propellant hydrazine engines (41.3 N per nozzle) spread engine exhaust over a wide angle, causing only modest surface erosion during landing (Mehta et al., 2011; Shorthill et al., 1976a; Shorthill et al., 1976b), and the depth of the residual crater with a radius of 50 cm from the engine centerline under the lander ranges from 1 to 4 cm (Hutton et al., 1980). A residual crater with 150 cm diameter and ~35 cm deep was excavated during the landing of Tianwen-1 with a high-thrust single-nozzle engine (~3000 N, about 23 times the thrust of the Phoenix/InSight's single nozzle). Further, as reported by Mehta et al. (2011), supersonic pulsed jets produce erosion rates more than an order of magnitude greater than those of other jet-induced processes. Thus, landing missions requiring high-thrust engines, such as crewed landing missions, non-pulsed thrusters could be the best choice. From the perspective of plume-surface interaction, it seems that the configuration with multiple nozzles is more advantageous to the landing safety, while the risk increases with the growth of the engine's number.

Tianwen-1 provide a unique dataset on the plume-surface interaction for the landing process with a high-thrust single-nozzle engine. In this work, we first report the plume impingement effects on the Martian surface induced by a high-thrust single-nozzle engine (~3000 N). Specifically, the impacted area and erosion volume of the landing area were estimated, and the dimensions of the residual crater under the lander were also measured. During the landing phase, we also looked at the evolution characteristics of the plume-Martian surface interaction and derived the weighted average depths and rates of infilling and erosion. The shallow stratigraphic architecture of the residual crater was investigated, too. These findings may serve future Mars missions, especially those using non-pulsed high-thrust engines. The planning of future Mars missions will benefit from the results of this study: (1) Our results can be used to constrain ground experiments and numerical simulations, such as the amount of impacted area and erosion volume in the landing area, the dimensions of the residual crater, and the average depths and rates of infilling and erosion during the landing phase. (2) The understanding of the evolution characteristics of plume-surface interaction can guide the design of the landing strategy, such as the selections of the optimal engine shut-off height, the hovering and obstacle avoidance height, and the terrain of the immediate touchdown area. Specifically, for a propulsion system similar to the Tianwen-1 lander, from the perspective of plume-surface interaction, the optimal engine shut-off height at approximately 3000 N thrust is about 15 m and the lander height during hovering and obstacle avoidance should be larger than about 31 m. In addition, the terrain of the immediate touchdown area can be selected to be relatively higher in the middle and lower around to try to avoid the plume-induced deep crater which may threaten the safety of the lander. As for the specific terrain parameters of the immediate touchdown area, it needs to be further investigated. (3) The zoning of the landing area (Zones ① to ④) can guide sampling site selections for future Mars sample-return missions. Besides, the surface regolith structure revealed by the production mechanism of the plume-induced light and dark surface patterns observed in the HiRISE image along with the shallow stratigraphic architecture exposed by the residual crater may be used to understand the planet's geological evolution, hydrological cycle, and palaeoclimate and palaeoenvironment.

The analysis shows that depressions and infilling are a complex process that changes patterns as the lander descends. The plume will seriously erode the area below the nozzle, causing a deep crater. Meanwhile, the radial flow tends to flatten the peripheral area of the lander, depending on the regolith homogeneity. When the lander is at a relatively large height, erosion is primarily driven by the VE. As the height of the lander decreases, a deep crater gradually forms in the area directly below the nozzle. As the crater gradually forms, erosion shifts to be dominated by the BCF, DDF, or a combination of the BCF and DDF. Because the thrust of the Tianwen-1 engine is large, the BCF/DDF process is more pronounced. In addition, the formation of the deep crater will also affect the exhaust gas flow field. This may change some particles' trajectories, resulting in these particles moving at high speeds toward the bottom of the lander. These high-speed particles may cause damage to the instruments at the bottom of the lander. Therefore, special protection is required for these instruments, particularly on future crewed missions with increased thrust.

However, there are still limitations to our analysis, as to the estimation of the total erosion volume. The effects of filling in ground depressions with material are not specifically considered in our analysis. The amount of infilling is affected by many factors, such as the flatness of the terrain and the distance from the lander. Because of the limited number and quality of terrain images from the NaTeCams, we cannot obtain a precise DEM of the landing area following the Tianwen-1 landing. Besides, a precise DEM of the landing area prior to touch down is not available. As a result, the volume of material filling in the depressions cannot be determined using a method similar to that in Subsection 2.1. Further, given that the final results yield a relatively large uncertainty margin, it is reasonable to assume that the estimation can tolerate the error caused by the effects of filling in depressions with material. At least, the volume calculated can be regarded as a lower limit of the total impacted volume. Moreover, the long intervals between the landing cameras' continuous shots have made it difficult to estimate in more detail the evolution of the plume's interaction with the Martian surface during the landing phase. Our results will, however, contribute to the implementation of future Mars missions. In addition, the estimation of the distribution of plume-induced regolith erosion rates on a geological time scale seems to be difficult. First, the total number of successful Mars landing missions is very limited. Further, the plume-induced erosion rate depends on various factors, such as the thrust and configuration of the engine. Tianwen-1 is the first Mars mission using a non-pulsed high-thrust single-nozzle engine while other successful Mars landing missions by NASA used pulsed/non-pulsed multiple-nozzle engines instead. Thus, the plume-induced erosion rates for these missions are difficult to compare quantitatively.

It is worth mentioning that the in-situ data of plume-surface interaction are also conducive to extracting the values of the mechanical properties of the surface regolith at the Tianwen-1 landing site by modeling, such as the internal friction angle and the cohesion. These mechanical properties are likely benefiting a preliminary study of the geological engineering (Liu et al., 2020; Griffiths and Lane, 1999; Han and Ma, 2019; Hao et al., 2022; Karaulov et al., 2022) on Mars. Our next target is to model the interaction between the plume and the Martian surface at the Tianwen-1 landing site.

Although these findings can deepen our understanding of the plume-surface interaction on Mars, they are still far from exhaustive: the range and precision of the reconstructed model are still confined due to the limited number and quality of the images collected. At present, the Tianwen-1 orbiter and the Zhurong rover are still in operation and continue collecting data. These data will form the basis of further investigations and hopefully shed further light on outstanding scientific issues.

## 4. Materials and methods

### *4.1. The landing camera dataset*

The pair of landing cameras are located at the lower edge of the circular chassis of the Tianwen-1 lander (Hua et al., 2022). They are symmetrically installed relative to the lander's engine nozzle center (Fig. 2C and Fig. S1). Their internal parameters, including the field of view, focal length, pixel resolution, principal point coordinate, and exposure time, are almost completely the same with a slight difference in the principal point coordinates (see supplementary materials for details). In addition, they can take pictures of the approaching terrain simultaneously during the slow landing phase of the lander. The dataset consists of four sets of grayscale images, two images in each set taken by the landing cameras simultaneously at four different lander heights, as shown in Fig. 2, A and C. Note that these images have been scaled with the corresponding lander heights when shooting. These high-resolution grayscale images can provide accurate information about the local landing terrain with an effective pixel number of 2048 × 2048. Of note here is that distortion corrections have been performed to these images beforehand. The brightness, color temperature, and contrast of the first three sets of images (Fig. 2A) are adjusted appropriately to facilitate the selection of feature points used to determine the lander height with the linear projection model. Since the field of view of the fourth set of images shown in Fig. 2C is severely obscured by rising dust, this set of images has been processed by low-pass filtering for denoising and smoothing.

### 4.2. The NaTeCams dataset

The NaTeCams are binocular stereo cameras mounted on the Zhurong rover, primarily providing support for the guidance, navigation, and control of the rover, including scientific observations (Liang et al., 2021). The NaTeCams are color imaging systems with complementary metal-oxide semiconductor-active pixel sensors. The fields of view of these cameras are 46.5°, and their depths of field range from 0.5 m to infinity with optimum focuses of 1.0 m (Liang et al., 2021). The NaTeCams dataset consists of color images with an effective pixel number of 2048 × 2048 and pixel resolution of 5.5 $\mu$m, providing relatively accurate terrain information, such as slope, undulation, roughness, etc. The dataset for the reconstruction of the DEM of the peripheral region of the lander consists of two sets, 24 images each collected by the NaTeCams on May 18 and 21, 2021 with low and high pitch angles shooting around, respectively, as shown in Fig. S3. As for the dataset for the reconstruction of the residual crater beneath the lander, it consists of 18 images shown in Fig. S5B. For more information about the NaTeCams, the reader can refer to the literature (Liang et al., 2021).

### 4.3. The RoPeR dataset

The principal goals of the RoPeR are to investigate the thickness of the upper Martian soil and the structure of potentially buried water-ice or dry ice, and to determine the depth distribution of the subsurface stratigraphy (Tan et al., 2021; Zhou et al., 2020). The device has two channels with different operating frequencies, namely the low-frequency channel (CH1) and the high-frequency channel (CH2). The CH1 antenna is mounted on the two sides of the bottom surface of the rover's top board. The CH2 antenna is mounted on the front board of the rover (Zhou et al., 2020). The RoPeR continuously scans the ground as the rover travels. The scanning data will provide the coordinates of the rover's location. Based on the coordinates of these scanning points, it can be deduced that the rover performs a scanning about every 5 cm of travel. More information about the RoPeR can be found in the literature (Tan et al., 2021; Zhou et al., 2020).

### 4.4. Data analysis

The study on the evolution of the interaction between the engine plume and the Martian surface is based on the DEMs of the touchdown areas at different lander heights reconstructed with the linear projection model using the landing images. Concerning the DEM reconstruction of the landing area, the DEM of the peripheral region of the lander is reconstructed based on the images collected by the NaTeCams and corrected according to the image from the HiRISE and the Zhurong rover's spatial data collected by the RoPeR, while the residual crater under the lander is reconstructed using the images taken by the NaTeCams around the lander after the rover landed. More details on the data analysis are given in the supplementary materials.

## Declaration of Competing Interest

The authors declare that they have no known competing financial interests or personal relationships that could have appeared to influence the work reported in this paper.

## Data availability

The Tianwen-1 datasets are available via the lunar and planetary data release system of the National Astronomical Observatories of China (NAOC) at website https://moon.bao.ac.cn/web/enmanager/home. All data needed to evaluate the conclusions in the paper are present in the paper and/or the Supplementary Materials.

## Acknowledgments

Scientific data of the Tianwen-1 mission are provided by the China National Space Administration (CNSA). We are grateful for the support from the team members of the Ground Research and Application System (GRAS), who contributed to data receiving and preprocessing. This work was supported by Space Optoelectronic Measurement & Perception Laboratory of BICE (Grant number LabSOMP-2021-04); the Pre-Research Project on Civil Aerospace Technologies of China National Space Administration (Grant number D020101); the Science and Technology Development Fund of Macau (Grant numbers 0089/2018/A3, 0049/2020/A1, 0014/2022/A1, and 008/2017/AFJ); the National Natural Science Foundation of China (Grant numbers 42004157, 41941001, and 11761161001); Key Laboratory Fund of Science and Technology on Vacuum Technology and Physics (Grant number 6142207200202), Youth Talent Promotion Project of Gansu Province (Grant number GXH20210611-05), and National Key Laboratory of Materials Behaviors and Evaluation Technology in Space Environments (Grant number WDZC-HGD-2022-08).

## Appendix A. Supplementary data

Supplementary data to this article can be found online at https://doi.org/10.1016/j.enggeo.2023.107278.

## References

Alexander, J.D., Roberds, W.M., Scott, R.F., 1966. Soil erosion by landing rockets.

Bagnold, R.A., 1941. The Physics of Blown Sand and Desert Dunes.

Bandfield, J.L., 2007. High-resolution subsurface water-ice distributions on Mars. Nature 447, 64–67. https://doi.org/10.1038/nature05781.

Ding, L., Zhou, R., Yu, T., Gao, H., Yang, H., Li, J., Di, K., 2022. Surface characteristics of the Zhurong Mars rover traverse at Utopia Planitia. Nat. Geosci. 15, 171–176. https://doi.org/10.1038/s41561-022-00905-6.

Fontes, D.H., Metzger, P.T., 2022. Rocket plume interacting with Mars soil particulates. In: AIAA SCITECH 2022 Forum.

Franz, H.B., Trainer, M.G., Malespin, C.A., Mahaffy, P.R., Atreya, S.K., Becker, R.H., Wong, M.H., 2017. Initial SAM calibration gas experiments on Mars: Quadrupole mass spectrometer results and implications. Planet. Space Sci. 138, 44–54. https://doi.org/10.1016/j.pss.2017.01.014.

Golombek, M., Kass, D., Williams, N., Warner, N., Daubar, I., Piqueux, S., Pike, W.T., 2020. Assessment of InSight landing site predictions. J. Geophys. Res.-Planets 125. https://doi.org/10.1029/2020JE006502.

Griffiths, D.V., Lane, P.A., 1999. Slope stability analysis by finite elements. Géotechnique 49, 387–403. https://doi.org/10.1680/geot.1999.49.3.387.

Han, J., Ma, Q., 2019. Finite element analysis of geotechnical excavation based on COMSOL multiphysics. IOP Conf. Ser.: Mater. Sci. Eng. 592, 012060 https://doi.org/10.1088/1757-899x/592/1/012060.

Han, Q.D., Liu, F., Pan, Y.L., Wang, H., Lan, X.H., Pan, K.Z., Wei, Q., 2022. Characteristics and flight performance of the Tianwen-1 Mars lander propulsion system. Sci. Sin. Technol. 52, 237–244. https://doi.org/10.1360/SST-2021-0481.

Hao, N., Li, X., Li, Y., Jia, J., Gao, L., 2022. A novel reliability-based method of calibrating safety factor: application to the cemented sand and gravel dams. Eng. Geol. 306, 106719 https://doi.org/10.1016/j.enggeo.2022.106719.

Harri, A.M., Genzer, M., Kemppinen, O., Kahanpaa, H., Gomez-Elvira, J., Rodriguez-Manfredi, J.A., Team, R.M.S., 2014. Pressure observations by the Curiosity rover: initial results. J. Geophys. Res.-Planets 119, 82–92. https://doi.org/10.1002/2013JE004423.

Hoey, W.A., Lam, R.L., Wong, A.T., Soares, C.E., 2020. Europa lander engine plume interactions with the surface and vehicle. 2020 Ieee Aerospace Conference (Aeroconf 2020). https://doi.org/10.1109/AERO47225.2020.9172679.

Horányi, M., Sternovsky, Z., Lankton, M., Dumont, C., Gagnard, S., Gathright, D., Wright, G., 2014. The lunar dust experiment (LDEX) onboard the lunar atmosphere and dust environment explorer (LADEE) mission. Space Sci. Rev. 185, 93–113. https://doi.org/10.1007/s11214-014-0118-7.

Hua, B., Li, T., Liu, Y., Wang, L., Zhang, Y., 2022. Evaluation for stereo vision hazard avoidance technology of Tianwen 1 lander. J. Astronaut. 43, 56–63. https://doi.org/10.3873/j.issn.1000-1328.2022.01.007.

Huang, X., Li, M., Wang, X., Hu, J., Zhao, Y., Guo, M., Xu, L., 2021. The Tianwen-1 guidance, navigation, and control for Mars entry, descent, and landing. Space: Sci. Technol. 2021, 9846185. https://doi.org/10.34133/2021/9846185.

Hutton, R.E., Moore, H.J., Scott, R.F., Shorthill, R.W., Spitzer, C.R., 1980. Surface erosion caused on Mars from Viking descent engine plume. Moon Planets 23, 293–305. https://doi.org/10.1007/BF00902045.

Immer, C., Metzger, P., Hintze, P.E., Nick, A., Horan, R., 2011. Apollo 12 Lunar Module exhaust plume impingement on Lunar Surveyor III. Icarus 211, 1089–1102. https://doi.org/10.1016/j.icarus.2010.11.013.

Karaulov, A.M., Korolev, K.V., Kuznetsov, A.O., 2022. Bearing capacity assessment of soil foundation. Soil Mech. Found. Eng. 59, 111–118. https://doi.org/10.1007/s11204-022-09790-y.

Kreslavsky, M.A., Head, J.W., 2002. Fate of outflow channel effluents in the northern lowlands of Mars: The Vastitas Borealis Formation as a sublimation residue from frozen ponded bodies of water. J. Geophys. Res.: Planets 107. https://doi.org/10.1029/2001JE001831, 4-1-4-25.

Krupenio, N.N., 1977. Estimation of the density of Martian soil from radiophysical measurements in the 3-centimeter range. NASA-TM-75047.

Lane, J.E., Metzger, P.T., 2015a. Estimation of Apollo lunar dust transport using optical extinction measurements. Acta Geophys. 63, 568–599. https://doi.org/10.1515/acgeo-2015-0005.

Lane, J.E., Metzger, P.T., 2015b. Image analysis based estimates of regolith erosion due to plume impingement effects. Earth Space 2014, 140–151.

Li, C., Zhang, R., Yu, D., Dong, G., Liu, J., Geng, Y., Ouyang, Z., 2021a. China's Mars exploration mission and science investigation. Space Sci. Rev. 217, 57. https://doi.org/10.1007/s11214-021-00832-9.

Li, C., Zuo, W., Wen, W., Zeng, X., Gao, X., Liu, Y., Ouyang, Z., 2021b. Overview of the chang'e-4 mission: opening the frontier of scientific exploration of the lunar far side. Space Sci. Rev. 217, 35. https://doi.org/10.1007/s11214-021-00793-z.

Li, C., Zheng, Y., Wang, X., Zhang, J., Wang, Y., Chen, L., Wu, F., 2022. Layered subsurface in Utopia Basin of Mars revealed by Zhurong rover radar. Nature 610, 308–312. https://doi.org/10.1038/s41586-022-05147-5.

Liang, X., Chen, W., Cao, Z., Wu, F., Lyu, W., Song, Y., Wang, L., 2021. The navigation and terrain cameras on the Tianwen-1 Mars rover. Space Sci. Rev. 217, 37. https://doi.org/10.1007/s11214-021-00813-y.

Liu, S., Su, Z., Li, M., Shao, L., 2020. Slope stability analysis using elastic finite element stress fields. Eng. Geol. 273, 105673 https://doi.org/10.1016/j.enggeo.2020.105673.

Liu, Y., Wu, X., Zhao, Y.-Y.S., Pan, L., Wang, C., Liu, J., Zou, Y., 2022. Zhurong reveals recent aqueous activities in Utopia Planitia, Mars. Sci. Adv. 8, eabn8555. https://doi.org/10.1126/sciadv.abn8555.

Luo, P., Zhang, X., Fu, S., Li, Y., Li, C., Cao, J., 2022. First measurements of low-energy cosmic rays on the surface of the lunar farside from Chang'E-4 mission. Sci. Adv. 8, eabk1760. https://doi.org/10.1126/sciadv.abk1760.

McEwen, A.S., Eliason, E.M., Bergstrom, J.W., Bridges, N.T., Hansen, C.J., Delamere, W. A., Weitz, C.M., 2007. Mars reconnaissance orbiter's high resolution imaging science experiment (HiRISE). J. Geophys. Res.: Planets 112. https://doi.org/10.1029/2005JE002605.

Mehta, M., Renno, N.O., Marshall, J., Rob Grover, M., Sengupta, A., Rusche, N.A., Smith, P.H., 2011. Explosive erosion during the Phoenix landing exposes subsurface water on Mars. Icarus 211, 172–194. https://doi.org/10.1016/j.icarus.2010.10.003.

Mehta, M., Sengupta, A., Renno, N.O., Van Norman, J.W., Huseman, P.G., Gulick, D.S., Pokora, M., 2013. Thruster plume surface interactions: Applications for spacecraft landings on planetary bodies. AIAA J. 51, 2800–2818. https://doi.org/10.2514/1.J052408.

Meng, Q., Wang, D., Wang, X., Li, W., Yang, X., Yan, D., Dong, J., 2021. High resolution imaging camera (HiRIC) on China's first Mars exploration Tianwen-1 mission. Space Sci. Rev. 217, 42. https://doi.org/10.1007/s11214-021-00823-w.

Metzger, P., Li, X., Immer, C., Lane, J., 2009a. ISRU implications for lunar and Martian plume effects. In: 47th AIAA Aerospace Sciences meeting including the New Horizons Forum and Aerospace Exposition..

Metzger, P.T., 2016. Rocket exhaust blowing soil in near vacuum conditions is faster than predicted by continuum scaling laws. Earth Space 2016, 58–66.

Metzger, P.T., Immer, C.D., Donahue, C.M., Vu, B.T., Latta, R.C., Deyo-Svendsen, M., 2009b. Jet-induced cratering of a granular surface with application to lunar spaceports. J. Aerosp. Eng. 22, 24–32. https://doi.org/10.1061/(ASCE)0893-1321(2009)22:1(24).

Metzger, P.T., Smith, J., Lane, J.E., 2011. Phenomenology of soil erosion due to rocket exhaust on the Moon and the Mauna Kea lunar test site. J. Geophys. Res.: Planets 116. https://doi.org/10.1029/2010JE003745.

Morris, A.B., Goldstein, D.B., Varghese, P.L., Trafton, L.M., 2012. Far field deposition of scoured regolith resulting from lunar landings. In: 28th International Symposium on Rarefied Gas Dynamics 2012, Vols. 1 and 2, 1501, pp. 1220–1227. https://doi.org/10.1063/1.4769681.

Plemmons, D.H., Mehta, M., Clark, B.C., Kounaves, S.P., Peach, L.L., Renno, N.O., Young, S.M.M., 2008. Effects of the Phoenix lander descent thruster plume on the Martian surface. J. Geophys. Res.-Planets 113, E00A11. https://doi.org/10.1029/2007je003059.

Scott, R.F., Ko, H.-Y., 1968. Transient rocket-engine gas flow in soil. AIAA J. 6, 258–264. https://doi.org/10.2514/3.4487.

Shorthill, R.W., Hutton, R.E., Moore, H.J., Scott, R.F., Spitzer, C.R., 1976a. Physical properties of the Martian surface from the viking 1 lander: preliminary results. Science 193, 805–809. https://doi.org/10.1126/science.193.4255.805.

Shorthill, R.W., Moore, H.J., Hutton, R.E., Scott, R.F., Spitzer, C.R., 1976b. The environs of Viking 2 lander. Science 194, 1309–1318. https://doi.org/10.1126/science.194.4271.1309.

Shorthill, R.W., Moore, H.J., Scott, R.F., Hutton, R.E., Liebes, S., Spitzer, C.R., 1976c. The "soil" of Mars (Viking 1). Science 194, 91–97. https://doi.org/10.1126/science.194.4260.91.

Sizemore, H.G., Mellon, M.T., Searls, M.L., Lemmon, M.T., Zent, A.P., Heet, T.L., Keller, H.U., 2010. In situ analysis of ice table depth variations in the vicinity of small rocks at the Phoenix landing site. J. Geophys. Res.: Planets 115. https://doi.org/10.1029/2009JE003414.

Smith, P.H., Tamppari, L.K., Arvidson, R.E., Bass, D., Blaney, D., Boynton, W.V., Zent, A. P., 2009. $H_2O$ at the Phoenix landing site. Science 325, 58–61. https://doi.org/10.1126/science.1172339.

Spray, J.G., 2016. Lithification mechanisms for planetary regoliths: the glue that binds. Annu. Rev. Earth Planet. Sci. 44, 139–174. https://doi.org/10.1146/annurev-earth-060115-012203.

Tan, X., Liu, J., Zhang, X., Yan, W., Chen, W., Ren, X., Li, C., 2021. Design and validation of the scientific data products for China's Tianwen-1 mission. Space Sci. Rev. 217, 69. https://doi.org/10.1007/s11214-021-00843-6.

Tanaka, K.L., 2005. Geology and insolation-driven climatic history of Amazonian north polar materials on Mars. Nature 437, 991–994. https://doi.org/10.1038/nature04065.

Tanaka, K.L., Robbins, S.J., Fortezzo, C.M., Skinner, J.A., Hare, T.M., 2014. The digital global geologic map of Mars: Chronostratigraphic ages, topographic and crater morphologic characteristics, and updated resurfacing history. Planet. Space Sci. 95, 11–24. https://doi.org/10.1016/j.pss.2013.03.006.

Vizcaino, J., Mehta, M., 2015. Quantification of plume-soil interaction and excavation due to the Mars Science Laboratory Sky Crane Descent Phase. In: 8th Symposium on Space Resource Utilization.

Wan, W., Yu, T., Di, K., Wang, J., Liu, Z., Li, L., Bao, S., 2021. Visual localization of the Tianwen-1 lander using orbital, descent and rover images. Remote Sens. 13, 3439. https://doi.org/10.3390/rs13173439.

Warner, N.H., Golombek, M.P., Ansan, V., Marteau, E., Williams, N., Grant, J.A., Banks, M., 2022. In Situ and orbital stratigraphic characterization of the InSight landing site—A type example of a regolith-covered lava plain on Mars. J. Geophys. Res.: Planets 127. https://doi.org/10.1029/2022JE007232.

Watkins, R., Metzger, P.T., Mehta, M., Han, D., Prem, P., Sibille, L., Radley, C.F., 2021. Understanding and mitigating plume effects during powered descents on the Moon and Mars. Bull. AAS 53. https://doi.org/10.3847/25c2cfeb.f9243994.

Wu, X., Liu, Y., Zhang, C., Wu, Y., Zhang, F., Du, J., Zou, Y., 2021. Geological characteristics of China's Tianwen-1 landing site at Utopia Planitia, Mars. Icarus 370, 114657. https://doi.org/10.1016/j.icarus.2021.114657.

Ye, B., Qian, Y., Xiao, L., Michalski, J.R., Li, Y., Wu, B., Qiao, L., 2021. Geomorphologic exploration targets at the Zhurong landing site in the southern Utopia Planitia of Mars. Earth Planet. Sci. Lett. 576, 117199 https://doi.org/10.1016/j.epsl.2021.117199.

Ye, Q., Rao, W., Liu, F., Sun, Z., Liu, G., Wang, C., Lu, H., 2022. Interaction between engine plume and Martian soil during Mars landing. Acta Aeronaut. Astronaut. Sin. 43, 626557. https://doi.org/10.7527/s1000-6893.2021.26557.

You, J., Zhang, X., Zhang, H., Li, C., Xu, Y., Yan, Q., Zhi, Q., 2021. Analysis of plume–lunar surface interaction and soil erosion during the Chang'E-4 landing process. Acta Astronaut. 185, 337–351. https://doi.org/10.1016/j.actaastro.2021.05.009.

Zhao, J., Xiao, Z., Huang, J., Head, J.W., Wang, J., Shi, Y., Wang, L., 2021. Geological characteristics and targets of high scientific interest in the Zhurong landing region on Mars. Geophys. Res. Lett. 48 https://doi.org/10.1029/2021GL094903.

Zhou, B., Shen, S., Lu, W., Liu, Q., Tang, C., Li, S., Fang, G., 2020. The Mars rover subsurface penetrating radar onboard China's Mars 2020 mission. Earth Planet. Phys. 4, 345–354. https://doi.org/10.26464/epp2020054.

Zurek, R.W., Smrekar, S.E., 2007. An overview of the Mars Reconnaissance Orbiter (MRO) science mission. J. Geophys. Res.: Planets 112. https://doi.org/10.1029/2006JE002701.